Spectromicroscopy for Addressing the Surface and Electron Transport Properties of Individual 1-D Nanostructures and Their Networks

Andrei Kolmakov,[†,]* Sai Potluri,[†] Alexei Barinov,[‡] Tevfik O. Menteş,[‡] Luca Gregoratti,[‡] Miguel A. Niño,[‡] Andrea Locatelli,[‡] and Maya Kiskinova[‡]

[†]Southern Illinois University at Carbondale, Carbondale, Illinois 62901-4401, and [‡]Sincrotrone Trieste, 34012 Basovizza-Trieste, Italy

Implementation of "bottom-up" paradigm in technology is based on fabrication and assembly of artificial objects with dimensions ranging from a few to a few hundred nanometers with predesigned functionalities. Semiconducting quasi-one-dimensional (quasi-1D) nanostructures, in particular metal oxide (MOx) nanowires and nanobelts, are among the most promising platforms for gas sensing, energy harvesting/conversion, and opto-electronic applications.[1−3] When the effective diameter of these objects shrinks to the nanoscale, the surface starts to play a significant role and can even dominate their properties. For example, the attractive novel properties of semiconducting metal oxide nanowires in gas sensing[4−8] and electronically tunable reactivity[9,10] have been attributed to the intimate coupling between surface redox processes and electron concentration inside the nanostructure. In order to control this surface ↔ electron transport interplay and to develop a reproducible nanodevice, the fundamental relations between the surface composition, morphology, and electronic structure of oxide nanostructures along with their physical and chemical properties have to be identified. The complexity and challenges in such studies are dictated by two major factors: (i) the purity (both surface and bulk) and (ii) the strong size and morphology dependence of the observed phenomena. In addition, the substrate and electrodes in the real world devices can induce significant changes to the electronic properties of the nanostructure. Therefore, it is desirable to measure individual and prewired nanostructures since the results obtained on en-

ABSTRACT Understanding size/dimensionality-dependent phenomena and processes relevant to chemical sensing and catalysis requires analytical methods with high *surface* sensitivity, which can exploit the structure and composition of nanomaterials at their natural length scales and working conditions. In the present study, we explored the potentials and complementary capabilities of several surface-sensitive microscopy approaches to shed light on the properties of individual SnO$_2$ nanowires and their networks. Our results demonstrate the unique opportunities provided by synchrotron-based photoelectron microscopies for surface-sensitive structural and chemical analysis, including *in situ* characterization of electron transport properties of a nanostructure wired as an active element in chemiresistor devices.

KEYWORDS: SnO$_2$ nanowires · nanobelts · surface · electron spectroscopy · microscopy · PEEM · LEEM · SPEM · LEED · gas sensors · catalysis

sembles (bundles, films, *etc.*) lack size and morphology specificity.

Up to date, the structural and compositional *ex situ* and *in situ* characterization of the oxide nanostructures has exclusively been performed by means of scanning electron microscopy (SEM) or transmission electron microscopy (TEM).[11,12] The imaging and analytical capabilities, combined with the latest developments of sample stages in these machines, have allowed *in situ* exploration of the mechanical, compositional, electrical, and other properties of the nanostructures, as well as high-resolution imaging and analysis at elevated pressures and temperatures. Both techniques provide very high spatial resolution, but their spectroscopic abilities, based on energy-filtered electron and photon emission, such as electron energy loss, auger electron, and energy dispersive X-ray spectroscopy, are limited in energy resolution and/or *surface* sensitivity.

Alternative spectromicroscopy methods with surface sensitivity are those using X-ray sources and detecting photoelectrons
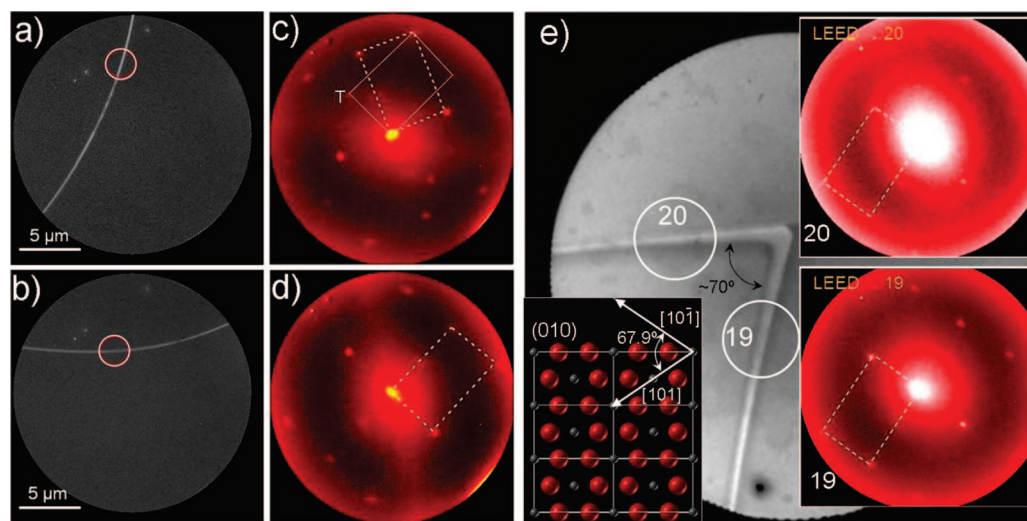
Figure 1. (a,b) Two LEEM images (FOV 20 μm) and (c,d) corresponding (1 × 1) LEED patterns collected from the two areas (marked with white circles) along the individual nanostructure. The rotation of the (1 × 1) LEED patterns approximately follows the bending of the nanostructure in real space. (e) LEEM (FOV 6 μm, 5.5 eV) image of the "kinked" nanostructure and (1 × 1) LEED patterns (45 eV) collected from different "arms". In spite of the changed orientation in the real space, the surface structure and its orientation are preserved along the length of the nanostructure. The inset depicts the model of the (010) facet and crystallographically equivalent growth directions.

emitted from the top few layers of the specimen. In these X-ray photoelectron microscopies, information for the chemical state and electronic structure of the surface is provided by the two well-developed spectroscopic methods: (i) X-ray photoelectron spectroscopy (XPS), which uses monochromatic photons to obtain energy distribution curves of the photoelectrons emitted from discrete atomic electron levels,[13] and (ii) X-ray absorption near-edge spectroscopy (XANES), where the total electron yield spectra are measured while varying the photon energy around the X-ray absorption thresholds corresponding to a given core electron binding energy.[14] Along with the surface chemical sensitivity, another advantage of these photoelectron-based spectroscopies is that the radiation damage, which can induce irreversible structural and chemical changes in the nano-object, is weaker using X-rays relative to the electron beam. Probing the matter at submicrometer length scales using XPS and/or XANES requires the intense and tunable X-rays provided at the third generation synchrotron facilities. The spatial resolution is achieved using two different approaches, which classify the microscopies as scanning and full-field imaging.[15−17] In the scanning photoelectron microscopy (SPEM), the incident photon beam is demagnified to a submicrometer (*ca.* 100−200 nm) spot onto the sample, which can be raster scanned with respect to the microprobe. In the X-ray photoelectron emission microscopies (XPEEM), a magnified image of the irradiated area is obtained by projection of the emitted electrons using appropriate electron tailoring optics. These synchrotron-based microscopies can be successfully complemented with conventional surface science methods for structural analysis, as low energy electron diffraction (LEED) and low energy electron microscopy

(LEEM). In fact, an important advantage of XPEEM instruments is the possibility to perform LEEM in the same setup,[18] which provide complementary morphological information with spatial resolution of 10 nm and microspot LEED monitoring the long-range atomic order from an area of 1−2 μm. SPEM and XPEEM have successfully been used for analysis of C and MoS_x nanotubes,[19−25] GaN nanowire,[26] oxide nanoparticles, and wires.[27,28] A few experimental impediments for PEEM imaging and spectroscopy on an individual prewired nanowire chemiresistor were reported in our previous work,[29] and some solutions were proposed.

This communication reports on the surface structure, composition, and morphology of *individual* quasi-1D SnO_2 nanostructures, their percolating networks, and corresponding transport properties when they are indexed as a part of the device. The results, obtained by combining surface-sensitive spectromicroscopy and transport measurement methods, provide new important information for these nanomaterials. The surface and sensor properties of the macroscopic counterparts selected for this study of SnO_2 nanostructures are already well-known,[30] and we have developed fabrication and handling protocols, which preserve their surface cleanliness (see ref 31 and supporting material therein).

RESULTS AND DISCUSSION

The SPEM and X-PEEM/LEEM experiments were performed at the ESCAmicroscopy[32] and Nanospectroscopy beamlines[17] at ELETTRA synchrotron radiation facility, hosting the SPEM and XPEEM-LEEM instruments, respectively. The XPEEM-LEEM is equipped with a hemispherical electron analyzer, reaching an energy resolution of 200 meV, and provides the complementary spec-

troscopic methods XANES and XPS. The lateral resolution is 10 nm in LEEM operation mode and a few tens of nanometers in energy-filtered X-PEEM imaging. The instrument can also perform micro-LEED and micro-XPS measurements, restricted to an area of 2 μm in diameter.

Surface Structure of the Individual Nanostructure. Figure 1a,b depicts LEEM images of two different parts of the *same* SnO_2 nanowire (here we are using the general term "nanowire" since the resolution is not sufficient to distinguish between nanostructures with different morphologies). Panels c and d represent the micro-LEED patterns collected at two locations (marked with white circles in a and b). Moving the sample in front of the LEEM objective, we were able to monitor the evolution of LEED patterns along the nanostructure's length. Both 1×1 micro-LEED patterns, marked by the white dashed line, correspond to a rutile surface unit cell with real space dimensions, $(3.23 \pm 0.1$ Å$) \times (4.88 \pm 0.12$ Å$)$, in agreement with the ones from (010) or (100) facets of the SnO_2 rutile crystals.[33] Soley on the basis of the LEED pattern, it is not possible to discriminate between these two facets. However, on the basis of previous HRTEM results showing that the preferable growth direction is [101] and (101)/(010) top/side faceting of SnO_2 rutile nanobelts and nanowires with rectangular cross section,[34] most probably the LEED pattern corresponds to a (010) side facet of the nanowire. This assignment is supported by the facile bending of the nanowire/nanobelt in this plane and the appearance of weaker diffraction spots in the LEED pattern. The latter ones are evidence of the single twin structure in the nanowire/nanobelt. Very similar SAED patterns, taken along the [010] zone axis, have been previously reported[34] for large diameter nanobelts, which agree well with our assignment.

Another class of quasi-1D nanostructures, explored by LEED, is nanowires which change their growth direction due to perturbed growth conditions while *preserving* their crystallographic orientation. In contrast to the nanobelt case, the V-shaped ("kinked") nanostructure in Figure 1e shows the same LEED pattern *independently* of the position. This observation corroborates nicely with previous HRTEM studies of the segmented and zigzag SnO_2 nanostructures, which have shown that such structures are in fact "sculptured" single crystals and their growth axis can be altered into crystallographically equivalent directions by tiny changes in the growth conditions.[35,36] Again, the LEED pattern in Figure 1e corresponds to the (010) facet of the nanostructure. Assuming that the growth takes place along the [10$\bar{1}$] and [101] directions, the angle at the kink is expected to be 67.9°, in agreement with the experimentally determined value of ~70°.

XANES and XPS on Individual Nanostructures. Figure 2 shows the XANES spectrum (green top line) of the SnO_2 nanobelt, measured with X-PEEM by collecting stacks
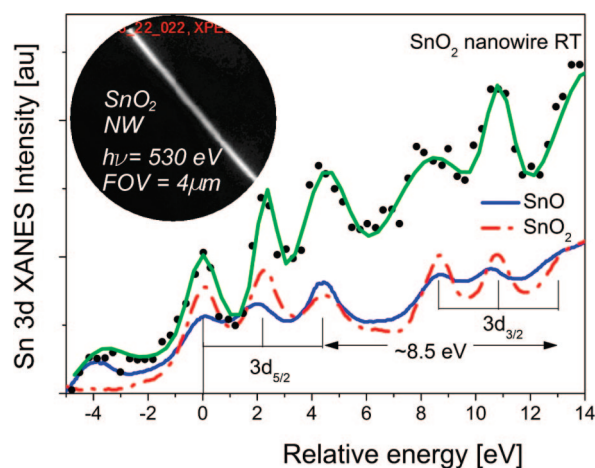

Figure 2. XANES spectrum (green) taken at room temperature on an individual SnO_2 nanowire obtained as a ratio of the gray scale signals form XPEEM (inset) images of the nanowire and background while scanning the photon energy from 480 to 505 eV. For comparison, XAS spectra from bulk SnO (blue) and SnO_2 (red) (adapted from ref 36) are shown. The energy scale is offset with respect to the first maximum of Sn $3d_{5/2}$.

of images while scanning the photon energy around the Sn 3d edge. For comparison, the XANES spectra of rutile SnO_2 (red) and tetragonal SnO (blue) samples, reported in ref 37, are also shown. Analogous to the macroscopic counterparts, the XANES spectrum from the individual nanostructure consists of the Sn $3d_{5/2}$ and $3d_{3/2}$ features (separated by ~8.5 eV), giving rise to six major transitions into the unoccupied Sn electronic states. Close inspection of the three spectra in Figure 2 reveals that in spite of the general similarity there are some differences in the relative intensity and shape of the nanobelt peaks, most evident in the 3−4 eV range. The enhanced relative intensity of the 4.2 eV peak, reported previously in ref 37, has been attributed to oxygen deficiency, induced by surface reconstruction. Since our LEED patterns do not evidence a reconstruction, this suggests that the nanobelt surface is partially reduced and the spectrum contains overlapping features of the SnO_2 and SnO phases, as indicated in the figure.

More detailed information for the surface chemical state has been obtained from the photoelectron spectra of individual SnO_2 nano(meso)structures, measured by SPEM, where the incident photon beam is *focused* to a small spot (100−200 nm). SPEM can be operated in two modes: (i) imaging by collecting photoelectrons within a selected kinetic energy window (Figure 3a), while scanning the sample with respect to the focused beam, and (ii) conventional energy dispersive electron spectroscopy from the illuminated local spot (micro-XPS) (Figure 3b−d). When the element under consideration is present in a single chemical state, the spatial variation in the contrast of the images reflects the variation of the photoelectron yield, which is a measure of the local concentration of the element. Figure 3a shows the Sn 4d image of a SnO_2 nanobelt (bright) placed on
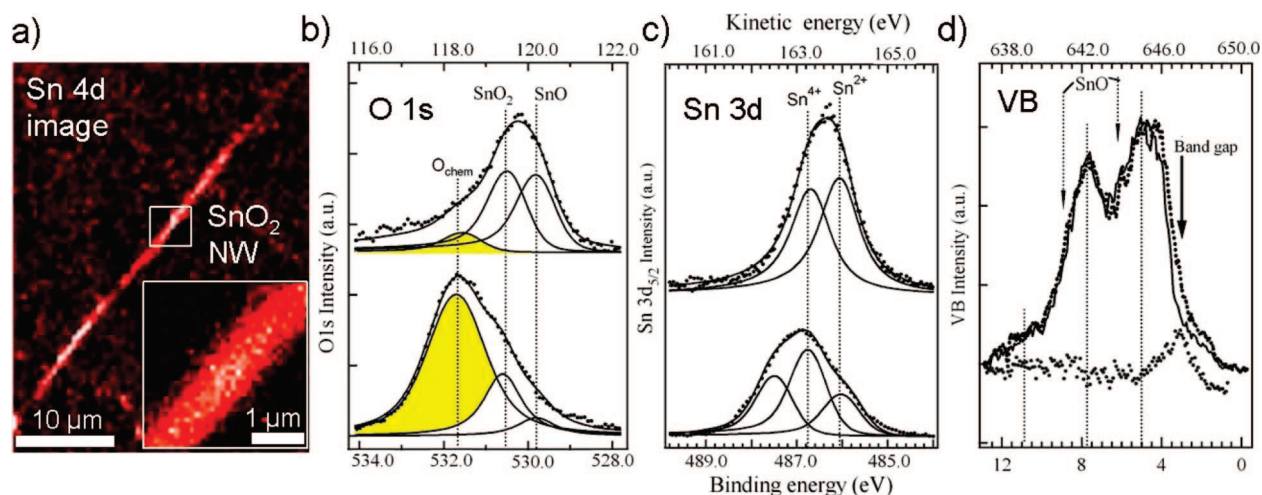
Figure 3. (a) Large- and small-scale chemical image of an individual SnO$_2$ nanobelt obtained by monitoring the Sn 4d photoelectrons. (b) O 1s, (c) Sn 3d$_{5/2}$, and (d) VB spectra taken from the SnO$_2$ nanobelt after oxygen plasma treatment (bottom spectrum in each panel, measured at room temperature) and after annealing at 523 K (top spectrum in each panel, measured at 523 K). The SnO band gap peak resulting from subtraction of the bottom from the top VB spectrum is shown by the dashed line in panel d.

a gold support (dark). Figure 3b shows two representative sets of O 1s, Sn 3d$_{5/2}$, and VB spectra measured on microspots of a freshly oxygen-plasma-treated nanostructure (bottom spectra) and after annealing to 523 K in UHV (top spectra). The spectra are deconvoluted considering the reported binding energy of Sn 3d$_{5/2}$ and O 1s core levels of SnO and SnO$_2$ macroscopic polycrystalline and single-crystal samples.[38−41] The presence of SnO-derived components in the O 1s and Sn 3d$_{5/2}$ spectra is in accordance with the XANES spectra in Figure 2. This should be attributed to lattice oxygen deficiency and reduced oxygen concentration at the surface, becoming more prominent after annealing to 523 K. The spectra from the fresh oxygen-plasma-treated sample have a weaker SnO component and contain also a third high BE component, which dominates the O 1s spectra. According to the literature,[41] the rather broad component at ∼531.7 eV (marked with yellow in Figure 3b) apparently originates from chemisorbed O-containing species, such as O$^{\delta-}$, O$_2$$^{\delta-}$, or OH$^{\delta-}$. Correspondingly, the high BE component in the Sn 3d$_{5/2}$ spectra can tentatively be attributed to surface Sn atoms bound to adsorbed species, resulting in O coordination higher than that in SnO$_2$. The relatively high intensity of the "O$_{chem}$" component is due to the very high surface sensitivity, resulting from the low kinetic energy of the O 1s and Sn 3d$_{5/2}$ photoelectrons and the grazing acceptance geometry of the energy analyzer in SPEM. The origin of this component is confirmed by its strong attenuation due to desorption upon annealing to 523 K. The O$_{chem}$ component also gradually loses intensity under prolonged X-ray irradiation at room temperature due to photon-induced desorption, whereas the oxide components remain practically intact. The VB spectra in Figure 3d are measured with a lower surface sensitivity due to the high photoelectron kinetic energy. They are dominated by the SnO$_2$ main

peaks centered at ∼5, 8, and 11 eV, originating from the O(2p) nonbonding, Sn(5s)−O(2p), and Sn(5p)−O(2p) states, respectively, whereas the SnO-related features at ∼3, 6.5, and 9.7 eV are appearing as weak shoulders.[42] The only distinct difference in the VB spectra of a fresh and annealed nanostructure is the increase of the emission at ∼3 eV, attributed to Sn(5s−5p)-hybridized states in the SnO band gap.[37,41] It is clearly manifested by the VB spectral difference shown by the dashed line in panel d. These results support that the oxygen deficiency is mostly at the surface and, due to the larger probing depth, is not very evident in the VB spectra.

Addressing the Electron Transport in a Working Device. When the SnO$_2$ nanostructures are wired as active elements in nanodevices, their electronic and surface properties cannot be fully decoupled from effects induced by other parts of the nanodevice such as electrodes, support, *etc*. Some examples of possible effects on the nanowire properties are the electrostatically controlled reactivity,[43] the gate-induced electrodesorption,[10] and the influence of the mobile parasitic charges on the transport properties.[44] In order to get insight into how these phenomena affect the electronic status of the nanostructures, wired as part of a device, the analytical measurements have to be performed under conditions close or identical to the working ones. The straightforward application of the photoelectron spectromicroscopy to working nanodevices is generally hampered by parasitic charging since the standard device architectures routinely involve isolating layers or support in the proximity of the nanostructure.[45] One of the possible solutions is to use a model UHV-compatible device containing a suspended nanostructure similar to the one described in ref 29. For the present study, we fabricated a model chemiresistor gas sensing device using Si$_3$N$_4$ membranes with periodic 2 μm holes as a support me-
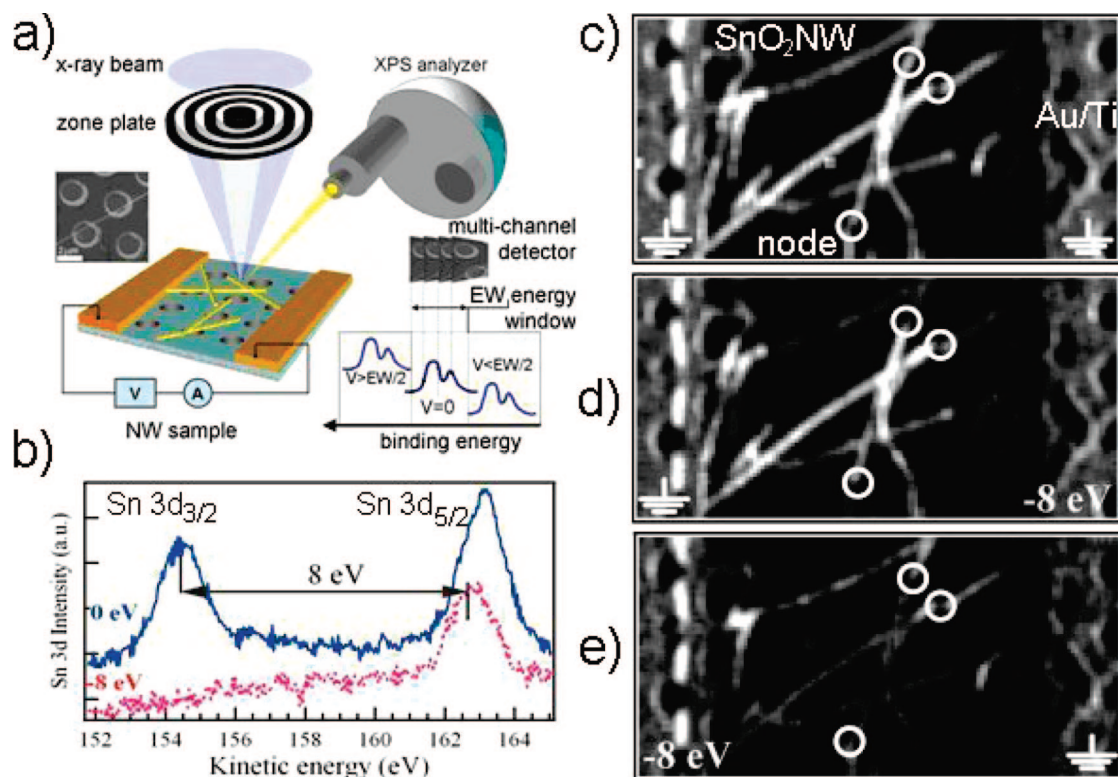
Figure 4. Spectromicroscopic access to the particularities of the electron transport and charge distribution in the working nanowire device. (a) Sketch of the experimental setup used for SPEM characterization of the SnO$_2$ nanowire mats under variable bias conditions. The images were measured over the energy window of Sn 4d emission. (b) The Sn 3d$_{3/2}$ and 3d$_{5/2}$ spectra taken in a selected spot of a nanowire, grounded (blue) and biased (red) by applying a potential of −8 V at the left electrode. (c,d) Sn 4d maps of the chemiresistor of percolating SnO$_2$ nanowires taken with both electrodes grounded (c), with the right (d) or left (e) electrode biased at −8 V. The differences between the images of "nonbiased" and "biased" structures indicate the parts of the nanowire network that are biased, resulting in a drop of the photoemission intensity due to shift of the Sn 4d emission outside the energy window. The dependence of the electron yield on the biased electrode side is due to the presence of highly resistive nodes (marked with white circles) which impede even potential distribution along the nanowire network, so that only the nanostructures which remain at ground potential are bright.

dia for the nanowire network (Figure 4a). The size of the holes is an order of magnitude larger than the X-ray microprobe of SPEM, which allows the nanowires placed over the holes to be locally probed. The SPEM experimental setup for imaging the SnO$_2$ nanowire network contacted by two electrodes is depicted in Figure 4a. For this setup, the conductivity between the electrodes has a percolating character and depends sensitively on the gas environments and on the density and transport quality of the straight parts of the nanowires and their junctions (nodes).[44] Under such conditions, the energy position and the width of the photoelectron spectra can be affected by external bias, band bending, and/or local electrostatic potential at the irradiated point. For zero bias voltage, the magnitude of the steady-state potential depends on the conductivity and electron yield, which is a function of the photon flux, photoionization cross section, and secondary electron emission. For low conductive materials, since the screening of the created electron holes is not sufficient, the electron emission results in local positive charging, which results in reducing the kinetic energy of the emitted photoelectron with the same value. Since the "disturbed" sample volume by the X-ray-

induced electron emission is of the order of ~50 nm, apparently the screening becomes an issue with reducing the dimensions of the semiconducting oxide structure. In fact, for the measurements described in previous sections, the whole nanostructure is placed on a grounded Au foil, the contact with which provides the electrons for screening the created electron holes. Thus the Sn 3d$_{5/2}$ and O 1s spectra in Figures 2 and 3 appear at binding energies identical to that measured for the extended materials. For the transport experiments, only one side of the nanowire is in contact with the grounded gold electrode. Due to the low conductivity and significant length of the nanowires, the screening of the core holes is not sufficient anymore and the corresponding Sn 3d spectrum in Figure 4b (blue line) is shifted to a lower kinetic (high binding) energy by ~0.5 eV, compared to the fully screened spectrum. This shift is constant, and we used the position of the Sn 3d$_{3/2}$ spectrum as a reference to examine the effect of the local potential on the kinetic energy of the emitted electrons. The bottom Sn 3d$_{3/2}$ spectrum, shifted by 8 eV to higher kinetic energy, was measured after applying exactly −8 eV potential to the electrode (the Sn 3d$_{5/2}$ peak has moved outside the displayed energy win-

dow). Since all emitted photoelectrons undergo the same potential-induced kinetic energy shift, the position (and presence) of core level peak (*i.e.*, Sn 3d, 4d used in this study) in the energy window of the analyzer depends on local electrostatic potential of the probed area. The potential of SPEM for analyzing the charge distribution and transport properties of working nanodevices, based on the demonstrated correlation between the applied potential and kinetic energy of the emitted photoelectrons is best illustrated by the SPEM images in Figure 4c−e. They show a percolating nanowire network measured under three different biasing conditions. The energy window of 7.8 eV was tuned around the Sn 4d emission of nonbiased nanowires, which appear as bright stripes in Figure 4c. On the left and right side of the image, the metal electrodes are also distinct due to the intense secondary electron emission. The biasing of the right or left electrode (Figure 4d,e) results in very strong attenuation of the photoelectron signal (due to energy shift beyond the Sn 4d energy window) only from certain SnO$_2$ wires, which depends on the biased electrode. By close inspection of the images in Figure 4c,d, one can identify some wires with rather good conductivity, which remain visible and confined points (nods) of the high resistivity where nearly all potential drops and the entire group of nanowires disappear from the image up to the junction point. As can be expected by biasing (Figure 4e) of the opposite electrode, a complementing part of the network becomes visible again up to the same junction points.

SPEM, LEEM, and LEED, we obtained new information about the composition and structure of individual metal oxide nanowires and their 2D networks. The micro-LEED patterns obtained for the first time on individual SnO$_2$ nanowires confirm the (010) structure of the side facets and the preservation of the single-crystal orientation of the "kinked" nanostructures. Micro-XPS and XANES measured from the individual nanowires and nanobelts reveal surface stoichiometry, coordination, and oxidation state of the nanostructures similar to their macroscopic counterparts. Being extremely important for electronic screening effects, apparently 100 nm size domain is still too large to induce measurable size effects. The potential of SPEM to explore electron transport in the working chemiresistor device composed of mats of the percolating nanowires has allowed us to identify the presence of "electroactive" elements which control the transport through the entire percolating nanowire network. This approach opens new avenues to explore the surface structural and electronic properties of individual nanostructures as a function of nanostructure size, morphology, type of adsorbate, and temperature. In addition, we have shown that the method is applicable to the nanostructures wired as an active element of the functioning nanodevice (chemiresistor in our case). The latter offers a unique experimental platform for *in situ* and in real time studies in order to link fundamental surface processes taking place on the nanowire surface with the corresponding electronic and transport properties.

SUMMARY

Using several powerful spectromicroscopy and microscopy surface science tools, namely, X-PEEM,

METHODS

Pristine single-crystal quasi-1D SnO$_2$ nanowires and nanobelts were synthesized from SnO at *ca.* 1220 K in Ar flux (35 sccm) using the vapor−solid (VS) growth protocol. As-prepared nanostructures, with diameters and lengths in the range of 100−500 nm and 10−300 μm, correspondingly, were transferred from the alumina crucible and dry deposited on (i) a clean Si (111) wafer with native oxide layer for X-PEEM/LEEM measurements and (ii) a Au foil for SPEM characterization. A model nanodevice, which allows *in situ* SPEM characterization under biasing conditions, was prepared placing the 2D network of cross-linked SnO$_2$ nanowires on a perforated Si$_3$N$_4$ membrane (with periodic 2 μm holes (Aquamarijn Micro Filtration BV)) and evaporating on top of the nanowire network a few Au/Ti electrodes through a shadow mask. The distance between electrodes was *ca.* 20 μm. The average density of the nanowires in the network was **r** ∼ 0.036 μm^{-2}, which was close to the percolation threshold **r** ∼ 0.04 μm^{-2}. This SnO$_2$ nanowire/Si$_3$N$_4$ unit was placed and wire bonded in a ceramic chip holder. Wet processing (as those used in resist-based lithography) is avoided because it can contaminate the surface of the nanostructure and support and affect chemical and transport properties. The small amount of weakly bound C-containing species on nanostructure and device surfaces is unavoidable when the materials are in air (see survey XPS in ref 31). They are cleaned by brief annealing in vacuum and by oxygen plasma treatment before SPEM and X-PEEM/LEEM measurements. In particular, the sample was annealed at 530 K for a few minutes using indirect electron bombardment heating on the back side of the Au support. The oxygen flux was provided from a TECTRA radio frequency plasma source providing O flux of the order of 10^{15} atoms cm^{-2} min^{-1}.

REFERENCES AND NOTES

1. Lieber, C. M. Nanoscale Science and Technology: Building a Big Future From Small Things. *MRS Bull.* **2003**, *28*, 486–491.
2. Xia, Y. N.; Yang, P. D.; Sun, Y. G.; Wu, Y. Y.; Mayers, B.; Gates, B.; Yin, Y. D.; Kim, F.; Yan, Y. Q. One-Dimensional Nanostructures: Synthesis, Characterization, and Applications. *Adv. Mater.* **2003**, *15*, 353–389.
3. Wang, Z. L. Functional Oxide Nanobelts: Materials, Properties and Potential Applications in Nanosystems and Biotechnology. *Annu. Rev. Phys. Chem.* **2004**, *55*, 159–196.
4. Cui, Y.; Wei, Q. Q.; Park, H. K.; Lieber, C. M. Nanowire Nanosensors for Highly Sensitive and Selective Detection

of Biological and Chemical Species. *Science* **2001**, *293*, 1289–1292.

5. Law, M.; Kind, H.; Messer, B.; Kim, F.; Yang, P. D. Photochemical Sensing of NO_2 with SnO_2 Nanoribbon Nanosensors at Room Temperature. *Angew. Chem., Int. Ed.* **2002**, *41*, 2405–2408.

6. Comini, E.; Faglia, G.; Sberveglieri, G.; Pan, Z. W.; Wang, Z. L. Stable and Highly Sensitive Gas Sensors Based on Semiconducting Oxide Nanobelts. *Appl. Phys. Lett.* **2002**, *81*, 1869–1871.

7. Kolmakov, A.; Zhang, Y. X.; Cheng, G. S.; Moskovits, M. Detection of CO and O_2 Using Tin Oxide Nanowire Sensors. *Adv. Mater.* **2003**, *15*, 997–1001.

8. Zhang, D. H.; Liu, Z. Q.; Li, C.; Tang, T.; Liu, X. L.; Han, S.; Lei, B.; Zhou, C. W. Detection of NO_2 Down to ppb Levels Using Individual and Multiple In_2O_3 Nanowire Devices. *Nano Lett.* **2004**, *4*, 1919–1924.

9. Zhang, Y.; Kolmakov, A.; Lilach, Y.; Moskovits, M. Electronic Control of Chemistry and Catalysis at the Surface of an Individual Tin Oxide Nanowire. *J. Phys. Chem. B* **2005**, *109*, 1923–1929.

10. Fan, Z. Y.; Lu, J. G. Gate-Refreshable Nanowire Chemical Sensors. *Appl. Phys. Lett.* **2005**, *86*, 123510–123513.

11. Wang, Z. L. New Developments in Transmission Electron Microscopy for Nanotechnology. *Adv. Mater.* **2003**, *15*, 1497–1514.

12. Bell, D. C.; Wu, Y.; Barrelet, C. J.; Gradecak, S.; Xiang, J.; Timko, B. P.; Lieber, C. M. Imaging and Analysis of Nanowires. *Microsc. Res. Tech.* **2004**, *64*, 373–389.

13. Siegbahn, K. From X-ray to Electron-Spectroscopy and New Trends. *J. Electron Spectrosc. Relat. Phenom.* **1990**, *51*, 11–36.

14. Stohr, J. *NEXAFS Spectroscopy*; Springer Series in Surface Sciences 25, Springer Verlag: Berlin, 1992.

15. Gunther, S.; Kaulich, B.; Gregoratti, L.; Kiskinova, M. Photoelectron Microscopy and Applications in Surface and Materials Science. *Prog. Surf. Sci.* **2002**, *70*, 187–260.

16. Frazer, B. H.; Girasole, M.; Wiese, L. M.; Franz, T.; De Stasio, G. Spectromicroscope for the Photoelectron Imaging of Nanostructures with X-rays SPHINX: Performance in Biology, Medicine and Geology. *Ultramicroscopy* **2004**, *99*, 87–94.

17. Locatelli, A.; Aballe, L.; Mentes, T. O.; Kiskinova, M.; Bauer, E. Photoemission Electron Microscopy with Chemical Sensitivity: SPELEEM Methods and Applications. *Surf. Interface Anal.* **2006**, *38*, 1554–1557.

18. Bauer, E. LEEM Basics. *Surf. Rev. Lett.* **1998**, *5*, 1275–1286.

19. Chiou, J. W.; Yueh, C. L.; Jan, J. C.; Tsai, H. M.; Pong, W. F.; Hong, I. H.; Klauser, R.; Tsai, M. H.; Chang, Y. K.; Chen, Y. Electronic Structure of the Carbon Nanotube Tips Studied by X-ray Absorption Spectroscopy and Scanning Photoelectron Microscopy. *Appl. Phys. Lett.* **2002**, *81*, 4189–4191.

20. Goldoni, A.; Larciprete, R.; Gregoratti, L.; Kaulich, B.; Kiskinova, M.; Zhang, Y.; Dai, H.; Sangaletti, L.; Parmigiani, F. X-ray Photoelectron Microscopy of the C 1s Core Level of Free-Standing Single-Wall Carbon Nanotube Bundles. *Appl. Phys. Lett.* **2002**, *80*, 2165–2167.

21. Suzuki, S.; Watanabe, Y.; Ogino, T.; Heun, S.; Gregoratti, L.; Barinov, A.; Kaulich, B.; Kiskinova, M.; Zhu, W.; Bower, C.; *et al.* Extremely Small Diffusion Constant of Cs in Multiwalled Carbon Nanotubes. *J. Appl. Phys.* **2002**, *92*, 7527−7531.

22. Suzuki, S.; Watanabe, Y.; Ogino, T.; Heun, S.; Gregoratti, L.; Barinov, A.; Kaulich, B.; Kiskinova, M.; Zhu, W.; Bower, C.; *et al.* Electronic Structure of Carbon Nanotubes Studied by Photoelectron Spectromicroscopy. *Phys. Rev. B* **2002**, *66*, 035414−035418.

23. Hong, I. H.; Chiou, J. W.; Wang, S. C.; Klauser, R.; Pong, W. F.; Chen, L. C.; Chuang, T. J. Electronic Structure of Aligned Carbon Nanotubes Studied by Scanning Photoelectron Microscopy. *J. Phys. IV* **2003**, *104*, 467–470.

24. Suzuki, S.; Watanabe, Y.; Ogino, T.; Homma, Y.; Takagi, D.; Heun, S.; Gregoratti, L.; Barinov, A.; Kiskinova, M. Observation of Single-Walled Carbon Nanotubes by Photoemission Microscopy. *Carbon* **2004**, *42*, 559–563.

25. Kovac, J.; Zalar, A.; Remskar, M.; Mrzel, A.; Mihailovic, D.; Gregoratti, L.; Kiskinova, M. Elettra Highlights. lnww.elettra.trieste.it/science/highlights/index.html, 2003.

26. Chiou, J. W.; Jan, J. C.; Tsai, H. M.; Pong, W. F.; Tsai, M. H.; Hong, I. H.; Klauser, R.; Lee, J. F.; Hsu, C. W.; Lin, H. M.; *et al.* Electronic Structure of GaN Nanowire Studied by X-ray-Absorption Spectroscopy and Scanning Photoelectron Microscopy. *Appl. Phys. Lett.* **2003**, *82*, 3949−3951.

27. Nolting, F.; Luning, J.; Rockenberger, J.; Hu, J.; Alivisatos, A. P. A PEEM Study of Small Agglomerates of Colloidal Iron Oxide Nanocrystals. *Surf. Rev. Lett.* **2002**, *9*, 437–440.

28. Xiao, Y.; Cai, Z.; Wang, Z. L.; Lai, B.; Chu, Y. S. An X-ray Nanodiffraction Technique for Structural Characterization of Individual Nanowires. *J. Synchrotron Radiat.* **2005**, *12*, 124–128.

29. Kolmakov, A.; Lanke, U.; Karam, R.; Shin, J.; Jesse, S.; Kalinin, S. V. Application of Spectromicroscopy Tools to Explore Local Origins of Sensor Activity in Quasi-1D Oxide Nanostructures. *Nanotechnology* **2006**, *17*, 4014–4018.

30. Batzill, M.; Diebold, U. The Surface and Materials Science of Tin Oxide. *Prog. Surf. Sci.* **2005**, *79*, 47–154.

31. Sysoev, V.; Goschnick, J.; Schneider, T.; Strelcov, E.; Kolmakov, A. A Gradient Microarray Electronic Nose Based on Percolating SnO_2 Nanowire Sensing Elements. *Nano Lett.* **2007**, *7*, 3182–3188.

32. Gregoratti, L.; Barinov, A.; Benfatto, E.; Cautero, G.; Fava, C.; Lacovig, P.; Lonza, D.; Kiskinova, M.; Tommasini, R.; Mahl, S.; *et al.* 48-Channel Electron Detector for Photoemission Spectroscopy and Microscopy. *Rev. Sci. Instrum.* **2004**, *75*, 64−69.

33. Batzill, M.; Katsiev, K.; Burst, J. M.; Diebold, U.; Chaka, A. M.; Delley, B. Gas-Phase-Dependent Properties of SnO_2 (110), (100), and (101) Single-Crystal Surfaces: Structure, Composition, and Electronic Properties. *Phys. Rev. B* **2005**, *72*.

34. Dai, Z. R.; Gole, J. L.; Stout, J. D.; Wang, Z. L. Tin Oxide Nanowires, Nanoribbons, and Nanotubes. *J. Phys. Chem. B* **2002**, *106*, 1274–1279.

35. Duan, J. H.; Gong, J. F.; Huang, H. B.; Zhao, X. N.; Cheng, G. X.; Yu, Z. Z.; Yang, S. G. Multiform Structures of SnO_2 Nanobelts. *Nanotechnology* **2007**, *18*, 055607–055613.

36. Lilach, Y.; Zhang, J. P.; Moskovits, M.; Kolmakov, A. Encoding Morphology in Oxide Nanostructures during Their Growth. *Nano Lett.* **2005**, *5*, 2019–2022.

37. Kucheyev, S. O.; Baumann, T. F.; Sterne, P. A.; Wang, Y. M.; van Buuren, T.; Hamza, A. V.; Terminello, L. J.; Willey, T. M. Surface Electronic States in Three-Dimensional SnO_2 Nanostructures. *Phys. Rev. B* **2005**, *72*, 035404–035410.

38. Themlin, J. M.; Chtaib, M.; Henrard, L.; Lambin, P.; Darville, J.; Gilles, J. M. Characterization of Tin Oxides by X-ray-Photoemission Spectroscopy. *Phys. Rev. B* **1992**, *46*, 2460–2466.

39. Szuber, J.; Czempik, G.; Larciprete, R.; Koziej, D.; Adamowicz, B. XPS Study of the L-CVD Deposited SnO_2 Thin Films Exposed to Oxygen and Hydrogen. *Thin Solid Films* **2001**, *391*, 198–203.

40. Kwoka, M.; Ottaviano, L.; Passacantando, M.; Santucci, S.; Czempik, G.; Szuber, J. XPS Study of the Surface Chemistry of L-CVD SnO_2 Thin Films After Oxidation. *Thin Solid Films* **2005**, *490*, 36–42.

41. Nagasawa, Y.; Choso, T.; Karasuda, T.; Shimomura, S.; Ouyang, F.; Tabata, K.; Yamaguchi, Y. Photoemission Study of the Interaction of a Reduced Thin Film SnO_2 With Oxygen. *Surf. Sci.* **1999**, *435*, 226–229.

42. DePadova, P.; Larciprete, R.; Ottaviani, C.; Quaresima, C.; Perfetti, P.; Borsella, E.; Astaldi, C.; Comicioli, C.; Crotti, C.; Matteucci, M.; *et al.* Synchrotron Radiation Photoelectron Spectroscopy of the O 2s Core Level as a Tool for Monitoring the Reducing Effects of Ion Bombardment on SnO_2 Thin Films. *Appl. Surf. Sci.* **1996**, *104*, 349−353.

43. Zhang, Y.; Kolmakov, A.; Chretien, S.; Metiu, H.; Moskovits, M. Control of Catalytic Reactions at the Surface of a Metal Oxide Nanowire by Manipulating Electron Density Inside It. *Nano Lett.* **2004**, *4*, 403–407.

44. Kalinin, S. V.; Shin, J.; Jesse, S.; Geohegan, D.; Baddorf, A. P.; Lilach, Y.; Moskovits, M.; Kolmakov, A. Electronic Transport Imaging in a Multiwire SnO$_2$ Chemical Field-Effect Transistor Device. *J. Appl. Phys.* **2005**, *98*, 044503.

45. Gunther, S.; Kolmakov, A.; Kovac, J.; Kiskinova, M. Artefact Formation in Scanning Photoelectron Emission Microscopy. *Ultramicroscopy* **1998**, *75*, 35–51.